Low bandgap high entropy alloy for visible light-assisted photocatalytic degradation of pharmaceutically active compounds

Shubhasikha Das[a], M. Sanjay[b], Abhay Raj Singh Gautam[c], Rakesh Behera[c], Chandra Sekhar Tiwary[b]*, Shamik Chowdhury[a]*

[a]School of Environmental Science and Engineering,
Indian Institute of Technology Kharagpur, West Bengal 721302, India

[b]Department of Metallurgical and Materials Engineering,
Indian Institute of Technology Kharagpur, West Bengal 721302, India

[b]Department of Materials Engineering,
Indian Institute of Technology Gandhinagar, Gujarat 382055, India

* Corresponding author.

E-mail address: chandra.tiwary@metal.iitkgp.ac.in (C. S. Tiwary)
shamikc@iitkgp.ac.in (S. Chowdhury)

ABSTRACT

The incessant accumulation of pharmaceutically active compounds (PhACs) in various environmental compartments represents a global menace. Herein, an equimolar and environmentally benign FeCoNiCuZn HEA is synthesized via a facile and scalable method, and its effectiveness in eliminating four different PhACs from aqueous matrices is rigorously examined. Attributing to its relatively low bandgap and multielement active sites, the as-synthesized quinary HEA demonstrates more pronounced photocatalytic decomposition efficiency, towards tetracycline (86%), sulfamethoxazole (94%), ibuprofen (80%), and diclofenac (99%), than conventional semiconductor-based photocatalysts, under visible light irradiation. Additionally, radical trapping assays are conducted, and the dissociation intermediates are identified, to probe the plausible photocatalytic degradation pathways. Further, the end-products of FeCoNiCuZn-mediated photocatalysis are eco-friendly, and the HEA can be successfully recycled repeatedly, with no obvious leaching of heavy metal ions. Overall, the findings of this study testify the applicability of FeCoNiCuZn HEA as a visible light-active photocatalyst, for treating wastewaters contaminated with PhACs.

Keywords: pharmaceuticals, heterogeneous photocatalysis, high entropy alloys, visible light, photocatalytic degradation mechanism

1. Introduction

With intensifying human therapeutic activities, especially in the wake of the ongoing COVID-19 pandemic, pharmaceutical residues from prescription and over-the-counter medicines are now ubiquitous in freshwater ecosystems across the globe [1-3]. This represents a major environmental and public health concern, attributed to their chronic as well as acute toxicological impacts, both on humans as well as aquatic organisms, even in very low concentrations [4-7]. Pharmaceutical substances in aqueous matrices originate primarily from human consumption, via excretion of both metabolized and unmetabolized drugs, as well as incorrect disposal of unused medicines, usually by flushing down the toilet/sink or by discarding them into waste bins destined for landfills [8,9]. As conventional wastewater treatment plants are largely ineffective at eliminating pharmaceutically active compounds (PhACs) from wastewaters, because of their inherent design limitations [2], there is an ever-mounting need for advanced technologies to minimize pharmaceutical release into the environment.

To that end, a wide array of techniques has been extensively tested in recent years, for the removal of PhACs from the effluents of pharmaceutical manufacturing facilities and hospital wastewaters. These range from physical (adsorption, dialysis, electrodialysis, evaporation, filtration, flocculation, reverse osmosis, sedimentation, and stream stripping) and chemical processes (ion-exchange, neutralization, reduction, precipitation, advanced oxidation, and calcination), to biological treatment methods (activated sludge, aerated lagoons, anaerobic digestion, trickling filters, and waste stabilization ponds) [2]. Amongst these, advanced oxidation via heterogeneous photocatalysis has garnered tremendous scientific attention, attributing to its ability to exploit sunlight as a renewable energy resource, as well as a multitude of competitive advantages: (i) operational simplicity, (ii) robustness, (iii) near-complete mineralization of contaminants, (iv)

scalability, and (v) low cost [10]. In light of the aforementioned merits, several diverse semiconducting materials, such as zinc oxide [11], ferric oxide [12], titanium dioxide [13], tungsten trioxide [14], bismuth tungstate [15], bismuth oxyhalides [16], metal organic frameworks [17], carbon quantum dots [18], carbon nitrides [19], transition metal dichalcogenides [20], and MXenes [21], have been rigorously evaluated for removing PhACs from aqueous solutions. However, the photocatalytic activity, and hence the on-site applications, of most of these photoresponsive semiconductors is restricted by several factors, such as insufficient absorption of solar radiation in the visible range, rapid recombination of the photogenerated charge carriers, and lack of adequate catalytically active sites.

As a promising alternative, high-entropy alloys (HEAs) are attracting a great deal of attention for a range of catalytic applications over the past few years [22]. HEAs are alloys comprising at least five principal metal atoms, usually in equiatomic or near equiatomic ratios [23]. The uniform mixing of multiple elements during their synthesis elevates the system entropy, producing an entropy-driven, thermodynamically, and kinetically stabilized structure [24], with a near-continuum of surface-active sites [25]. As the binding energy between an active site and a reactant molecule is also dictated by the interaction with adjacent atoms, each active site in a HEA is dissimilar because of diverse local environment of each element [26]. Further, the pronounced lattice distortion, induced by the atomic size difference of the individual components, can hypothetically diminish the adsorption energy as well as the activation barrier, leading to a desirable reaction rate [27]. Additionally, it can enhance the durability of HEAs to withstand harsh reaction conditions, such as elevated temperatures, corrosive chemicals, and extreme reaction environments, amongst others [28]. More interestingly, the multielement interactions in HEAs can give rise to unusual behaviors and properties as compared to atoms in single-element

materials [29]. In view of these unparalleled attributes, HEAs have gained unprecedented momentum over the last several years for use across diverse technologies. Especially in the context of heterogeneous photocatalysis, there exists almost unlimited opportunities to conceive new photocatalysts based on HEAs, with potentially elevated photocatalytic activities than contemporary semiconductor-based photocatalysts. However, to date, only a rare cohort of studies have strived or made genuine efforts to comprehend the photocatalytic potential of HEAs from the perspective of practical applications [30].

In order to fill this knowledge gap, herein a quinary (FeCoNiCuZn) HEA has been synthesized through a facile induction melting approach, and rigorously evaluated as photocatalyst for the decomposition of four representative PhACs (viz., tetracycline (TC), sulfamethoxazole (SMX), ibuprofen (IBP), and diclofenac (DCF)) under visible light irradiation. Iron (Fe), cobalt (Co), nickel (Ni), copper (Cu), and zinc (Zn) have been particularly chosen for preparing the HEA because of their relative abundance and low cost. More attractively, these heavy metals are highly prospective candidates for resource recovery from industrial wastewaters, and may, therefore, reduce the overall cost of the HEA, with a potential revenue benefit option. On the other hand, TC, SMX, IBP, and DCF were selected as proxies for PhACs due to their frequent occurrence in freshwater environments, inherent toxicity, and structural features similar to several other PhACs. Attributing to its significantly low bandgap of 1.32 eV, the as-synthesized FeCoNiCuZn HEA can degrade up to 86%, 94%, 80%, and 99% of TC, SMX, IBP, and DCF, respectively within 120 min of visible light exposure. In order to gain insights into the underlying photocatalytic degradation mechanism, the role of various reactive oxygen species, as well as the diverse intermediates formed during the photocatalytic reaction, are elucidated. Furthermore, the evaluation of the probable toxicity of the treated PhAC solutions reveals that the photocatalysis

end-products do not pose any conceivable public health threats. More importantly, the as-developed HEA demonstrates a relatively stable cycling performance for prolonged operation, without any significant metal leaching. To the best of our knowledge, this is the first report which describes in detail the application potential of equimolar HEA as photocatalyst for wastewater remediation. The outcomes of this study offer interesting insights into the rational design and development of more efficient HEAs for treating wastewater contaminated with PhACs via heterogenous photocatalysis.

2. Experimental

2.1. Materials

All four selected PhACs, isopropyl alcohol (IPA), sodium azide (NaN_3), potassium iodide (KI), ascorbic acid (AA), and absolute ethanol were procured from Sigma Aldrich. Phosphate buffered saline (PBS), nutrient agar, and nutrient broth were obtained from HiMedia. All chemicals and reagents were used as received without further purification. Distilled water (DI) was used throughout the experiments.

2.2. Synthesis of FeCoNiCuZn HEA powder

FeCoNiCuZn HEA was synthesized through induction melting, using high purity (>99.99%) metal chips. In brief, Fe, Co, Ni, Cu, and Zn chips were mixed in a stoichiometric ratio of 1:1:1:1:1, loaded into an alumina crucible, and melted in an induction furnace at 1250 °C for 10 min under an inert atmosphere. The obtained sample was then remelted in a muffle furnace at 1000 °C for 96 h to attain a single-phase structure, with homogenous composition. The resulting melt was then naturally cooled to room temperature, following which it was subjected to ball milling for 12 h in a planetary mill to obtain the FeCoNiCuZn HEA powder.

2.3. Characterization of FeCoNiCuZn HEA

Field emission gun-scanning electron microscopy (FEG-SEM) imaging was conducted on a Zeiss Supra 40 field emission gun-scanning electron microscope (Carl Zeiss SMT AG, Germany), equipped with INCA X-Sight energy-dispersive X-ray spectroscopy (EDX) detector (Oxford Instruments, United Kingdom). Transmission electron microscopy (TEM) images were captured on a FEI Titan Themis 60–300 cubed high-resolution transmission electron microscope (Field Electron and Ion Company, United States). X-ray diffraction (XRD) patterns were collected using a PANalytical X'pert PRO XRD system (Malvern PANalytical Ltd., Switzerland). The particle size distribution was determined using a Zetasizer Nano ZS90 analyzer (Malvern PANalytical Ltd., Switzerland. Raman spectral patterns were recorded with a Horiba T64000 triple-stage Raman spectrometer (Horiba Jobin Yvon Inc., France). Fourier transform infrared (FTIR) spectral fingerprints were acquired on a Bruker Alpha II FTIR spectrometer (Bruker Corporation, Germany). X-ray photoelectron spectroscopy (XPS) measurements were conducted using Thermo Scientific Nexsa surface analysis system (Thermo Fisher Scientific Inc., United States). Diffuse reflectance spectra were collected by an Analytik Jena Specord® S-600 UV/Vis spectrophotometer (Analytik Jena AG, Germany), coupled with an integrating sphere, using barium sulfate as the reflectance standard. The agar-well diffusion method was employed to assess the toxicity of the as-synthesized FeCoNiCuZn powder, towards the Gram-negative bacterium *Escherichia coli* (*E. coli*).

2.4. Photocatalytic experiments

The photocatalytic activity of the as-prepared FeCoNiCuZn HEA was examined for the degradation of four representative pharmaceutical pollutants (viz., TC, SMX, IBP, and DCF), at

25 °C in a 250 mL quartz triple-jacketed water-cooled immersion-type batch photochemical reactor (Lelesil Innovative Systems, India), under visible light illumination. A 450 W high-pressure mercury lamp, fitted with a UV cut-off filter ($\lambda < 420$ nm), was used as a visible light source. In a typical experiment, 50 mg of the FeCoNiCuZn powder was suspended onto the targeted PhAC (5 mg L^{-1}, 100 mL) solution. The suspension was then magnetically stirred without visible light exposure for 60 min in order to establish the adsorption/desorption equilibration. Thereafter, the reaction mixture was exposed to visible light and aliquots were withdrawn at pre-fixed time intervals. The extent of photocatalytic degradation was quantified using an UV/Vis spectrophotometer (UV Plus, Motras Scientific Instruments Pvt. Ltd., India) or an ultra-high-performance liquid chromatography (UHPLC) system (UltiMate 3000, Thermo Fisher Scientific Inc., United States). Specifically, the residual concentration of TC was estimated at the maximum absorbance wavelength of 358 nm. Meanwhile, the residual amount of SMX, IBP, and DCF was quantified with the aid of a diode array detector, set at a wavelength of 270 nm, 227 nm, and 220 nm respectively. Further, the photocatalytic degradation products were identified using a LTQ XL linear ion trap liquid chromatography-mass spectrometry (LCMS) system (Thermo Fisher Scientific Inc., United States). The photocatalytic degradation efficiency (%) of the FeCoNiCuZn powder at any time *t* after visible light irradiation was calculated according to the following equation:

$$\text{Photodegradation (\%)} = \frac{C_0 - C_t}{C_0} \times 100\% \quad (1)$$

where C_0 (mg L^{-1}) and C_t (mg L^{-1}) are the concentration of the PhAC in the test solution at $t = 0$ and $t = t$, respectively.

The degree of mineralization of the PhACs at the end of the irradiation period was determined by quantifying the total organic carbon (TOC) content (TOC-L analyzer, Shimadzu Corp., Japan), using the following equation:

$$\text{Mineralization (\%)} = \left(1 - \frac{[TOC]_t}{[TOC]_0}\right) \times 100\% \quad (2)$$

where $[TOC]_0$ (mg L^{-1}) and $[TOC]_t$ (mg L^{-1}) are the TOC of the test solution at $t = 0$ and $t = t$, respectively.

Additionally, the toxicity of the treated and untreated PhAC solutions was examined by analyzing the viability of *E. coli* cells using the standard plate count method. In brief, *E. coli* cells were pre-cultured in Luria–Bertani (LB) broth, then inoculated into either untreated or treated PhAC solution, and incubated under gentle shaking at 37 ^{o}C. An *E. coli* suspension in DI water was also prepared in a similar manner, but without any PhAC, as a control. After 24 h of incubation, each bacterial culture was diluted with PBS by a factor of 10^{-6}, employing the traditional serial dilution technique, and then spread evenly across the surface of LB agar plates, and incubated at 37 ^{o}C for 24 h. Subsequently, the number of colony forming units (CFUs) were counted and compared with the control plate to determine the potential toxicity of the byproducts, formed during the photocatalytic degradation of the targeted PhACs.

Finally, the reusability of the FeCoNiCuZn material was tested, from the viewpoint of practical applications, by conducting three successive photocatalytic cycles with the same batch of HEA. At the end of each cycle, the FeCoNiCuZn powder was directly removed from the test solution via filtration, washed with distilled water, oven dried, and resuspended onto fresh PhAC solution. Alongside, the leaching of metal ions (i.e., Fe^{2+}, Co^{2+}, Ni^{2+}, Cu^{2+}, and Zn^{2+}) from the HEA powder

into the reaction medium was investigated via inductively coupled plasma mass-spectrometry (ICP-MS) (iCAP RQ, Thermo Fisher Scientific Inc., United States).

3. Results and discussion

3.1. Characterization of FeCoNiCuZn HEA

FeCoNiCuZn powder was prepared from high purity elemental chips through induction melting and subsequent homogenization heat treatment, followed by ball milling, as illustrated in Fig. 1. The size distribution curve clearly depict that the average size of the synthesized particles is 256 nm (Fig. S1). FEG-SEM image of the as-developed quinary FeCoNiCuZn HEA shows equiaxed grain structure, with a nearly-spherical shape (Fig. 2a). Additionally, bright-field TEM image reveals that the particles are devoid of any clumping, individual metal clusters, or patches (Fig. 2c). The EDS elemental maps indicate that all the five elements in the HEA are uniformly distributed across the entire sample, with no indications of phase segregation (Fig. 2b). The homogenous distribution of the constituent elements at the atomic level is also confirmed through high-angle annular dark-field (HAADF) scanning TEM (Fig. 2d,e). Further, high-resolution TEM (HRTEM) image (Fig. 2f) and the corresponding fast Fourier transform (FFT) pattern (Fig. 2g) reflects the crystalline nature of the FeCoNiCuZn HEA. In particular, the distinct lattice fringes with an interplanar spacing of 0.21 nm, corresponds to the (111) crystallographic plane of face-centered cubic (*fcc*) structure (Fig. 2h). The latter is also corroborated by the appearance of (111) and (200) *fcc* peaks at 2θ of ~43° and ~51° in the XRD pattern (Fig. 3a). Besides, the absence of characteristic diffraction peaks of the individual elements ascertain that all the five metal atoms have been alloyed successfully into a single solid phase.

Subsequently, the surface chemistry of the quinary FeCoNiCuZn HEA was explored at room temperature, employing FTIR spectroscopy (Fig. 3b). The peak observed at 535 cm^{-1} is due to the Fe–O bond vibration [31,32]. The distinct band around 580 cm^{-1} may be ascribed to the Co–O stretching vibration [33]. The fairly sharp peaks at about 610, 548, and 624 cm^{-1} can be assigned to the stretching mode of Ni–O, Cu–O, and Zn–O bonds, respectively [34-36]. The detection of all the constituent elements in their oxide form can be attributed to the spontaneous oxidation of the FeCoNiCuZn surface when exposed to air [37]. Interestingly, this multimetallic oxide shell can yield synergistic properties, especially in terms of electronic conductivity, and therefore aid towards enhanced photocatalytic activity.

Additionally, the chemical oxidation state of the individual elements integrated within the quinary HEA was examined using XPS (Fig. 4). The appearance of the O 1s peak in the XPS survey spectrum can be credited to the formation of metal oxide layer on the outermost surface, which is consistent with the FTIR spectral interpretations, and can be substantiated by the valence state of the five metals. Fig. 4b presents the 2p core-state XPS spectrum for Fe. The deconvoluted 2p spectral band appearing at 724.6 eV ($2p_{1/2}$) is the characteristic peak of metallic Fe, while those at 712.4 and 719.7 eV can be indexed to Fe^{3+} ($2p_{3/2}$) and Fe^{2+}–Fe^{3+} species [37,38]. Meanwhile, deconvolution of the Co 2p spectrum indicates the presence of the metallic phase of Co at 778.1 eV ($2p_{3/2}$) and that of its Co^{2+} oxidation state at 780.8 ($2p_{3/2}$) and 796.6 eV ($2p_{1/2}$) (Fig. 4c) [39]. In addition, the satellite peaks at 784.4 and 802.4 eV imply the existence of mixed valence phases of Co [37]. In a similar way, the satellite peaks at 861.1 eV and 879.3 eV in the Ni 2p core-level XPS spectrum represent the mixed valence oxidation states of Ni (Fig. 4d) [37]. Further, the Ni 2p spectrum can be split into two separate peaks, centered at around 855.5 and 873.2 eV, which can be assigned to Ni^{2+} ($2p_{3/2}$) and Ni^{2+} ($2p_{1/2}$), respectively [39]. The Cu 2p spectrum can be well

fitted to three major components, ascribed to Cu^{+} $2p_{3/2}$ (932.4 eV), Cu^{+} $2p_{1/2}$ (952.5 eV), and mixed-valence Cu^{+}–Cu^{2+} compounds (934.1 eV) (Fig. 4e) [38]. Last but not the least, the 2p XPS spectrum of Zn can be fragmented into two prominent subpeaks (Fig. 4f). The peak at 1021.5 eV corresponds to Zn^{2+} $2p_{3/2}$, while that at 1044.6 eV can be attributed to Zn^{2+} $2p_{1/2}$ [40].

As the photocatalytic activity of any material depends extensively on its ability to absorb light, the UV/Vis absorbance spectrum of FeCoNiCuZn was recorded in diffuse reflectance mode and analyzed applying the Kubelka-Munk function. As evident from Fig. 3c, the as-synthesized quinary HEA particle exhibits strong absorption across the entire visible region of the electromagnetic spectrum, with no steep absorption edge. At room temperature, the bandgap energy, estimated by plotting the square root of the absorption coefficient versus photon energy (Fig. 3d), is found to be 1.32 eV. The narrow bandgap is likely to promote facile electron transfer from the valence band to the conduction band from thermodynamic point of view, and can, therefore, create adequate electron-hole pairs for driving photocatalytic reactions. Notably, these results establish the idea that increasing the complexity of an alloy, via the formation of HEA, is undeniably an effective strategy to design new photocatalysts, with potentially enhanced photocatalytic performance.

Besides, the toxic potential of FeCoNiCuZn was assessed against Gram-negative bacterium *E. coli* using the agar-well diffusion method, with the antibiotic ciprofloxacin as the positive control and PBS as the negative control. As seen in Fig. S2, ciprofloxacin significantly inhibits the proliferation of *E. coli* to an average diameter of 15 mm. On the other hand, there are no apparent zone of inhibition (ZOI) around the wells containing PBS or HEA, exemplifying the environmentally benign nature of FeCoNiCuZn.

3.2. Photocatalytic performance of FeCoNiCuZn HEA

3.2.1. Degradation of PhACs

The photocatalytic activity of the as-synthesized FeCoNiCuZn HEA was evaluated by investigating the degradation of four representative PhACs (i.e., TC, SMX, IBP, and DCF) under visible light irradiation in a batch photochemical reactor. Prior to the onset of the photocatalytic experiments, the test solution along with the HEA powder was stirred in the dark for 60 min, in order to attain adsorption−desorption equilibria. As can be seen in the 'Light OFF' phase of Fig. 5, up to 45%, 33%, 32%, and 38% of TC, SMX, IBP, and DCF is adsorbed, respectively by the FeCoNiCuZn material. The fairly high adsorption capacity of the HEA is likely to promote rapid diffusion of the pollutant molecules from the bulk solution to the particle surface, leading to a faster photocatalysis reaction rate. This is conceivable because photocatalysis is inherently a surface-driven phenomenon, and, therefore, the photocatalytic degradation potential of any photocatalyst is directly correlated to its adsorption characteristics [41-43]. Consequently, after 120 min of visible light illumination, a substantial fraction of all the PhACs is dissociated onto the surface of the FeCoNiCuZn, as evident from the 'Light ON' region of Fig. 5. In particular, the overall photocatalytic removal efficiency decreases according to the following sequence, DCF (99%) < SMX (94%) < TC (86%) < IBP (80%). However, in the absence of HEA powder, approximately 31%, 36%, 23%, and 19% of TC, SMX, IBP, and DCF is eliminated after 120 min of light exposure (Fig. S3), implying that direct photolysis has limited capability to disrupt the aromatic structure of the PhACs.

In order to further demonstrate the excellent photocatalytic degradation ability of the FeCoNiCuZn HEA powder, its PhAC removal capacity is compared to those of contemporary semiconductor-based photocatalysts (Table S1). It is observed that irrespective of the type of

pharmaceutical compound, their percentage decomposition over the as-developed FeCoNiCuZn HEA is several orders of magnitude higher than metal oxide nanoparticles and their composites, under similar experimental conditions. For instance, the visible light-assisted TC dissociation potential of FeCoNiCuZn is over 2.2 times of NiO [44]. Likewise, the percentage photocatalytic abatement of SMX, IBP, and DCF by the FeCoNiCuZn powder, under visible light illumination, is at least 4.7, 2.4, and 2-fold higher than that of ZnO [45], Co_3O_4 [46], and Fe_2O_3 [47], respectively. The superior photocatalytic performance of FeCoNiCuZn in comparison to most of the reference photocatalysts can be attributed to extensive absorption of visible light, because of its extremely narrow bandgap. Hand in hand, the unique polyelemental arrangement of FeCoNiCuZn offers a huge variety of active sites, which is essential to drive cascading phenomenon like heterogeneous photocatalysis. Beyond these considerations, the presence of plasmonic metal in the as-developed HEA, such as Cu with intense surface plasmon resonance in the visible region, can also promote the activation and transformation of pollutants.

3.2.2. Role of reactive oxygen species

It is widely accepted that several reactive oxygen species (ROS), such as superoxide radicals ($^{\bullet}O_2^-$), singlet oxygen ($^1O_2$), and hydroxyl radicals ($^{\bullet}OH$), are generated through the interaction of surface adsorbed oxygen (or water) with the photoinduced electrons and holes, which are the principal mediators of photocatalytic reactions, along with holes [48]. As such, elucidating the precise contribution of each ROS is pivotal for deciphering the underlying photocatalytic degradation mechanism. Hence, in the present study, radical-scavenging experiments were performed by spiking selected quenchers (20 mmol L^{-1}) into the reaction medium: ascorbic acid (AA) for $^{\bullet}O_2^-$ anions, sodium azide (NaN_3) for $^1O_2$, isopropyl alcohol (IPA) for $^{\bullet}OH$ radicals, and potassium iodide (KI) for holes. The scavenging agents were introduced just before the onset

of visible light irradiation, and their inhibitory effect on the photocatalytic activity of FeCoNiCuZn for the degradation of the targeted PhACs is collated in Fig. 6. In case of TC, IBF, and DCF (Fig. 6a,c,d), the addition of NaN_3, IPA, and KI into the reaction mixture shows miniscule impact on the FeCoNiCuZn-assisted photocatalytic degradation of the said PhACs. However, severe inhibition in the photocatalytic activity of the FeCoNiCuZn HEA is observed in the presence of AA, with only 31%, 39%, and 55% of TC, IBF, and DCF being degraded, respectively, after 120 min of visible light irradiation. Meanwhile, the percentage degradation of SMX is suppressed considerably upon the inclusion of IPA and KI, and drops even more sharply when AA is incorporated into the reaction mixture (Fig. 6b). Nevertheless, the inhibitory effects of IPA and KI are relatively less pronounced than those of AA. These findings conclusively suggest that regardless of the PhAC type, their photocatalytic decomposition over the synthesized FeCoNiCuZn HEA is primarily driven by $^{\bullet}O_2^-$ anions. However, $^{\bullet}O_2^-$ anion is not the exclusive ROS involved in the photocatalytic abatement of the PhACs, but is likely complemented by $^{\bullet}OH$ radicals and valence band holes, especially in the case of SMX.

Fig. 7 presents a plausible mechanism of FeCoNiCuZn-induced photocatalytic degradation of PhACs under visible light illumination. Based on the aforementioned results, it is conceivable that ROS formation by the synthesized HEA under visible light proceeds mainly via the one-electron reduction of molecular oxygen, as in equation 3.

$$O_2 + e^- \rightarrow {}^{\bullet}O_2^- \quad (3)$$

The reduced O_2, in the form of superoxide, can give rise to the non-radical ROS hydrogen peroxide (H_2O_2), which in the presence of photoinduced conduction band electrons yields the highly reactive hydroxyl radicals, as represented by equations 4 and 5, respectively.

$$^{\bullet}O_2^- + e^- + H^+ \rightarrow H_2O_2 \quad (4)$$

$$H_2O_2 + e^- \rightarrow {}^{\bullet}OH + OH^- \quad (5)$$

On the other hand, the photoinduced valence band holes can oxidize the surface adsorbed water to create hydroxyl radicals, as described by equation 6.

$$OH^- + h^+ \rightarrow {}^{\bullet}OH \quad (6)$$

Needless to say, the ROS thus generated (i.e., $^{\bullet}O_2^-$ and $^{\bullet}$OH radicals), as well as the photoinduced holes, eventually oxidize the PhACs, with the $^{\bullet}O_2^-$-induced oxidation route predominant over the $^{\bullet}$OH radical/hole attack pathway.

3.2.3. Photocatalytic degradation mechanism

In order to further clarify the photocatalytic degradation mechanism of the PhACs over the FeCuNiCoZn HEA under visible light irradiation, the dissociation intermediates were detected via LC-MS. In particular, the disintegration pathway of DCF was investigated in detail because of its maximum removal amongst all the four PhACs. A total of twelve compounds were identified for the photocatalytic degradation of DCF, as listed in Table S2, and the plausible dissociation mechanism is proposed in Fig. 8. In comparison with the parent compound, the intermediate with mass-to-charge ratio (*m*/*z*) of 251 can be ascribed to the direct decarboxylation of DCF to 2,6-dichloro-*N*-(2-methylphenyl) aniline (**1**), which upon subsequent oxidation by $^{\bullet}O_2^-$ or other oxidant yields 4-[(2,6-dichlorophenyl)amino]-3-methylphenol (*m*/*z* = 268) (**2**) [49]. Afterwards, dechlorination and oxidation of **2** leads to the formation of 2-(phenylamino)benzaldehyde (*m*/*z* = 196) (**3**) [50]. Additionally, **1** can also undergo dechlorination in response to ROS attack, resulting in 2-chloro-*N*-(2-methylphenyl) aniline (**4**) (*m*/*z* = 216). In an alternative route, 4-hydroxy diclofenac or 5-hydroxy diclofenac (*m*/*z* = 310) (**5**) is produced

via $^{\bullet}$OH radical initiated ring hydroxylation of DCF [51]. On further oxidation, these monohydroxylated intermediates are converted to 4-amino-3,5-dichlorophenol (**6**) (*m*/*z* = 177) through the cleavage of the C−N bond [52]. Apart from the aforementioned pathways, the direct oxidation of DCF by •OH radicals or photogenerated holes may result in the generation of 2,6-dichloroaniline (*m*/*z* = 160) (**7**) and 4-hydroxyphenylacetic acid (*m*/*z* = 153) (**8**), via the fracture of the C−N bond [53]. Upon successive oxidation by •OH radicals, the C−Cl bond dissociates, which in turn can transform 2,6-dichloroaniline to aniline (*m*/*z* = 93) (**9**) [54]. On the other hand, dehydroxylation of **8**, induced by •OH radical attack, may give rise to 2,5-dihydroxyphenylacetic acid (**10**) (*m*/*z* = 168). Eventually, all these intermediates are further acted upon by $^{\bullet}O_2^-$ and •OH, and broken into lower molecular weight and lesser aromatic moieties, such as hydroxyacetic acid (*m*/*z* = 75) (**11**) and prop-2-en-1-imine (*m*/*z* = 55) (**12**), or mineralized into CO_2, H_2O, NH_4^+, and NO_3^-. In fact, up to 39% TOC removal is achieved after 120 min of irradiation (Fig. S4), suggesting that DCF may be completely mineralized with extended reaction time.

3.2.4. Toxicity of the photocatalysis end-products

Even though the FeCoNiCuZn HEA exhibits enhanced photocatalytic activity for degradation of PhACs than contemporary semiconductor-based photocatalysts, complete mineralization is not achieved. Instead, several secondary residues are formed that may be even more toxic than the original pollutants. To that end, the toxicity of the primary PhACs and their corresponding degradation products on *E. coli* was assessed, employing the traditional CFU test. The results of the viable count assay are summarized in Fig. 9a-d. As can be seen, exposure to primary PhACs obviously leads to a massive drop in bacterial viability. For instance, less than 20% of the *E. coli* cells are viable after treatment with TC (5 mg L^{-1}) for 24 h (Fig. 9a). Similarly, the survival rate of *E. coli* is reduced to about 40%, when treated with 5 mg L^{-1} of DCF (Fig. 9d). Conversely,

the direct exposure of *E. coli* cells to a cocktail of degraded secondary products, generated from the same initial concentration of PhAC via FeCoNiCuZn-mediated photocatalysis, has little to no impact on their viability. The non-toxic effect of the secondary product mixture on bacteria can be ascribed to the photocatalytic degradation of the PhACs to less toxic secondary compounds. Further, the presence of numerous secondary residues may result in an antagonistic effect, manifesting in no observable toxicity. Alternatively, it may be noted that as the complex mixture of secondary residues is basically a concoction of an array of photocatalytically transformed products, the concentration of individual species in the mixture is apparently lower than that of the parental compound. Consequently, the mixture of secondary residues may induce either low-dose bacterial growth stimulation or dose-dependent toxicity. Nevertheless, the near-absence of bacterial toxicity upon treatment with the degraded products reaffirms the application potential of FeCoNiCuZn for treating wastewater contaminated with PhACs.

3.2.5. Stability and reusability of the photocatalyst

Along with phenomenal photocatalytic activity, the stability and reusability of any photocatalyst is critically important from the purview of practical applications. As such, the reusability of the FeCoNiCuZn HEA was investigated by conducting three consecutive photocatalytic runs with the same batch of the photocatalyst under identical conditions. Fig. 9e-f illustrates the cyclic photocatalytic performance of FeCoNiCuZn for the dissociation of various types of PhACs. Although there is a minor drop in the degradation efficiency after each round of photocatalysis, the HEA can still retain ~91%, ~95%, ~96%, and ~97% of its original activity for TC, SMX, IBP, and DCF, respectively, even at the end of the third cycle. Furthermore, the ICP-MS analyses of the test solutions suggest that there is no significant release of heavy metal ions from the HEA (Table 1). In particular, the leached concentrations of Fe^{2+}, Co^{2+}, Ni^{2+}, Cu^{2+}, and Zn^{2+} are

substantially lower than the discharge limit of heavy metal ions in inland surface water, as prescribed by the Central Pollution Control Board of India [55]. These findings clearly showcase the versatility and durability of the as-developed FeCoNiCuZn HEA for persistent application in wastewater treatment, without causing any secondary pollution.

4. Conclusion

In summary, an equimolar and environment friendly FeCoNiCuZn HEA, with single-phase and homogenous distribution of the constituent elements at the nanoscale, has been successfully synthesized through a facile and scalable induction melting approach. Photocatalytic degradation studies, performed in an immersion-type batch reactor, reveals that the as-prepared quinary HEA can effectively degrade a wide array of PhACs under visible light. Specifically, after 120 min of treatment, the photocatalytic removal efficiency decreases according to the following sequence, DCF (99%) < SMX (94%) < TC (86%) < IBP (80%), which is considerably higher than that of contemporary semiconductor-based photocatalysts. This in principle can be attributed to the narrow bandgap and multielement active sites of the FeCoNiCuZn HEA. Additionally, the results of radical scavenging tests and hole quenching assay suggest that superoxide anion and hydroxyl radical are the predominant ROS, contributing to the photocatalytic dissociation of the PhACs. Further, toxicity assessment of the treated PhAC solutions indicates that the photocatalysis end-products do not present any imminent threat to human health and environment. Most importantly, the as-developed FeCoNiCuZn HEA exhibit extraordinary stability for repeated usage over multiple reaction cycles. Overall, the present findings represent one of the first studies to demonstrate the application potential of equimolar HEAs as photocatalysts for eliminating PhACs from aqueous matrices.

Acknowledgements

Shubhasikha Das gratefully acknowledges the financial support provided by the Ministry of Education, Government of India for her doctoral study.

Appendix A. Supplementary information

Supplementary information associated with this article can be found in the online version.

References

[1] T. aus der Beek, F-A. Weber, A. Bergmann, S. Hickmann, I. Ebert, A. Hein, A. Küster, Pharmaceuticals in the environment – global occurrences and perspectives, Environ. Toxicol. Chem. 35 (2016) 823–835.

[2] M. Patel, R. Kumar, K. Kishor, T. Mlsna, C. U. Pittman Jr., D. Mohan, Pharmaceuticals of emerging concern in aquatic systems: chemistry, occurrence, effects, and removal methods, Chem. Rev. 119 (2019) 3510–3673.

[3] D. O'Flynn, J. Lawler, A. Yusuf, A. Parle-McDermott, D. Harold, T. Mc Cloughlin, L. Holland, F. Regan, B. White, A review of pharmaceutical occurrence and pathways in the aquatic environment in the context of a changing and the COVID-19 pandemic, Anal. Methods, 13 (2021) 575–594.

[4] H. K. Khan, M. Y. A. Rehman, R. N. Malik, Fate and toxicity of pharmaceuticals in water environment: an insight on their occurrence in South Asia, J. Environ. Manage. 271 (2020) 111030.

[5] J. Maculewicz, D. Kowalska, K. Świacka, M. Toński, P. Stepnowski, A. Białk-Bielińska, J. Dołżonek, Transformation products of pharmaceuticals in the environment: their fate, (eco)toxicity and bioaccumulation potential, Sci. Total Environ. 802 (2022) 149916.

[6] A. S. Adeleye, J. Xue, Y. Zhao, A. A. Taylor, J. E. Zenobio, Y. Sun, Z. Han, O. A. Salawu, Y. Zhu, Abundance, fate, and effects of pharmaceuticals and personal care products in aquatic environments, J. Hazard. Mater. 424 (2022) 127284.

[7] P. Vaudin, C. Augé, N. Just, S. Mhaouty-Kodja, S. Mortaud, D. Pillon, When pharmaceutical drugs become environmental pollutants: potential neural effects and underlying mechanisms, Environ. Res. 205 (2022) 112495.

[8] M. Ortúzar, M. Esterhuizen, D. R. Olicón-Hernández, J. González-López, E. Aranda, Pharmaceutical pollution in aquatic environments: a concise review of environmental impacts and bioremediation systems, Front. Microbiol. 13 (2022) 869332.

[9] H. de Oliveira Souza, R. dos Santos Costa, G. R. Quadra, M. A. dos Santos Fernandez, Pharmaceutical pollution and sustainable development goals: going the right way? Sustain. Chem. Pharm. 21 (2021) 100428.

[10] S. K. Loeb, P. J. J. Alvarez, J. A. Brame, E. L. Cates, W. Choi, J. Crittenden, D. D. Dionysiou, Q. Li, G. Li-Puma, X. Quan, D. L. Sedlak, T. D. Waite, P. Westerhoff, J.-H. Kim, The technology horizon for photocatalytic water treatment: sunrise or sunser? Environ. Sci. Technol. 53 (2019) 2937–2947.

[11] S. Majumder, S. Chatterjee, P. Basnet, J. Mukherjee, ZnO based nanomaterials for photocatalytic degradation of aqueous pharmaceutical waste solutions – a contemporary review, Environ. Nanotechnol. Monit. Manag. 14 (2020) 100386.

[12] A. H. Asif, S. Wang, H. Sun, Hematite-based nanomaterials for photocatalytic degradation of pharmaceuticals and personal care products (PPCPs): a short review, Curr. Opin. Green Sustain. Chem. 28 (2021) 100447.

[13] S. Murgolo, C. De Ceglie, C. Di Iaconi, G. Mascolo, Novel TiO_2-based catalysts employed in photocatalysis and photoelectrocatalysis for effective degradation of pharmaceuticals (PhACs) in water: a short review, Curr. Opin. Green Sustain Chem. 30 (2021) 100473.

[14] T. Velempini, E. Prabakaran, K. Pillay, Recent developments in the use of metal oxides for photocatalytic degradation of pharmaceutical pollutants in water – a review, Mater. Today Chem. 19 (2021) 100380.

[15] B. O. Orimolade, A. O. Idris, U. Feleni, B. Mamba, Recent advances in degradation of pharmaceuticals using Bi_2WO_6 mediated photocatalysis – a comprehensive review, Environ. Pollut. 289 (2021) 117891.

[16] P. Gao, Y. Yang, Z. Yin, F. Kang, W. Fan, J. Sheng, L. Feng, Y. Liu, Z. Du, L. Zhang, A critical review on bismuth oxyhalide based photocatalysis for pharmaceutical active compounds degradation: modifications, reactive sites, and challenges, J. Hazard. Mater. 412 (2021) 125186.

[17] C. Du, Z. Zhang, G. Yu, H. Wu, H. Chen, L. Zhou, Y. Zhang, Y. Su, S. Tan, L. Yang, J. Song, S. Wang, A review of metal organic framework (MOFs)-based materials for antibiotics removal via adsorption and photocatalysis, Chemosphere 272 (2021) 129501.

[18] M. Athulya, B. K. John, A. R. Chacko, C. Mohan, B. Mathew, A review on carbon quantum dot based semiconductor photocatalysts for the abatement of refractory pollutants, ChemPhysChem 23 (2022) e202100873.

[19] Y. Wang, B. Jing, F. Wang, S. Wang, X. Liu, Z. Ao, C. Li, Mechanism insight into enhanced photodegradation of pharmaceuticals and personal care products in natural water matrix over crystalline graphitic carbon nitrides, Water Res. 180 (2020) 115925.

[20] P. R. Sivaranjani, B. Janani, A. M. Thomas, L. L. Raju, S. S. Khan, Recent development in MoS_2-based nano-photocatalyst for the degradation of pharmaceutically active compounds, J. Clean. Prod. 352 (2022) 131506.

[21] I. Ihsanullah, MXenes as next-generation materials for the photocatalytic degradation of pharmaceuticals in water, J. Environ. Chem. Eng. 10 (2022) 107381.

[22] Y. Xin, S. Li, Y. Qian, W. Zhu, H. Yuan, P. Jiang, R. Guo, L. Wang, High-entropy alloys as a platform for catalysis: progress, challenges, and opportunities, ACS Catal. 10 (2020) 11280–11306.

[23] X. Wang, W. Guo, Y. Fu, High-entropy alloys: emerging materials for advanced functional applications, J. Mater. Chem. A 9 (2021) 663–701.

[24] Y. Yao, Z. Liu, P. Xie, Z. Huang, T. Li, D. Morris, Z. Finfrock, J. Zhou, M. Jiao, J. Gao, Y. Mao, J. Miao, P. Zhang, R. Shahbazian-Yassar, C. Wang, G. Wang, L. Hu, Computationally aided, entropy-driven synthesis of highly efficient and durable multi-elemental alloy catalysts, Sci. Adv. 6 (2020) eaaz0510.

[25] Y. Chen, X. Zhan, S. L. A. Bueno, I. H. Shafei, H. M. Ashberry, K. Chatterjee, L. Xu, Y. Tang, S. E. Skrabalak, Synthesis of monodisperse high entropy alloy nanocatalysts from core@shell nanoparticles, Nanoscale Horiz. 6 (2021) 231–237.

[26] T. Löffler, A. Ludwig, J. Rossmeisl, W. Schulmann, What makes high-entropy alloys exceptional electrocatalysts? Angew. Chem. Int. Ed. 60 (2021) 26894–26903.

[27] Y. F. Ye, Q. Wang, J. Lu, C. T. Liu, Y. Yang, High-entropy alloy: challenges and prospects, Mater. Today 19 (2016) 349–362.

[28] Y. Sun, S. Dai, High-entropy materials for catalysis: a new frontier, Sci. Adv. 7 (2021) eabg1600.

[29] S. Gao, S. Hao, Z. Huang, Y. Yuan, S. Han, L. Lei, X. Zhang, R. Shahbazian-Yassar, J. Lu, Synthesis of high-entropy alloy nanoparticles on supports by the fast moving bed pyrolysis, Nat. Commun. 11 (2020) 2016.

[30] T. Wang, Y. Wang, N. Wang, S. Xu, Z. Han, Y. Wang, Development of a novel $(Ni_{40}Fe_{30}Co_{20}Al_{10})_{90}Ti_{10}$ high-entropy alloy with excellent photocatalytic performance, Mater. Lett. 283 (2021) 128817.

[31] S. W. Hwang, A. Umar, G. N. Dar, S. H. Kim, R. I. Badran, Synthesis and characterization of iron oxide nanoparticles for phenyl hydrazine sensor applications, Sens. Lett. 12 (2014) 97–101.

[32] L. Zhang, M. Zhou, L. Shao, W. Wang, K. Fan, Q. Qin, Reactions of Fe with H_2O and FeO with H_2. A combined matrix isolation FTIR and theoretical study, J. Phys. Chem. A 105 (2001) 6998–7003.

[33] B. Pejova, A. Ishai, M. Najdoski, I. Grozdanov, Fabrication and characterization of nanocrystalline cobalt oxide thin films, Mater. Res. Bull. 36 (2001) 161–170.

[34] S. Sarkar, R. Sarkar, Synthesis, characterization and tribological study of zinc oxide nanoparticles, Mater. Today Proc. 44 (2021) 3606–3612.

[35] X. Zhang, J. Song, J. Jiao, X. Mei, Preparation and photocatalytic activity of cuprous oxides, Solid State Sci. 12 (2010) 1215–1219.

[36] Z. Wei, H. Qiao, H. Yang, C. Zhang, X. Yan, Characterization of NiO nanoparticles by anodic arc plasma method, J. Alloys Compd. 479 (2009) 855–858.

[37] E. Shen, X. Song, Q. Chen, M. Zheng, J. Bian, H. Liu, Spontaneously forming oxide layer of high entropy alloy nanoparticles deposited on porous carbons for supercapacitors, ChemElectroChem 8 (2021) 260–269.

[38] A. H. Phakatkar, M. T. Saray, M. G. Rasul, L. V. Sorokina, T. G. Ritter, T. Shokuhfar, R. Shahbazian-Yassar, Ultrafast synthesis of high entropy oxide nanoparticles by flame spray pyrolysis, Langmuir 37 (2021) 9059–9068.

[39] K. Huang, D. Peng, Z. Yao, J. Xia, B. Zhang, H. Liu, Z. Chen, F. Wu, J. Wu, Y. Huang, Cathodic plasma driven self-assembly of HEAs dendrites by pure single FCC FeCoNiMnCu nanoparticles as high efficient electrocatalysts for OER, Chem. Eng. J. 425 (2021) 131533.

[40] L. Sharma, N. K. Katiyar, A. Parui, R. Das, R. Kumar, C. S. Tiwary, A. K. Singh, A. Halder, K. Biswas, Low-cost high entropy alloy (HEA) for high-efficiency oxygen evolution reaction, Nano Res. 15 (2022) 4799–4806.

[41] S. Chowdhury, Y. Jiang, S. Muthukaruppan, R. Balasubramanian, Effect of boron doping level on the photocatalytic activity of graphene aerogels, Carbon 128 (2018) 237–248.

[42] Y. Jiang, S. Chowdhury, R. Balasubramanian, New insights into the role of nitrogen-bonding configurations in enhancing the photocatalytic activity of nitrogen-doped graphene aerogels, J. Colloid Interface Sci. 534 (2019) 574–585.

[43] Y. Jiang, S. Chowdhury, R. Balasubramanian, Efficient removal of bisphenol A and disinfection of waterborne pathogens by boron/nitrogen codoped graphene aerogels via the synergy of adsorption and photocatalysis under visible light, J. Environ. Chem. Eng. 8 (2020) 104300.

[44] Q. Yang, E. Guo, Q. Lu, M. Wei, J. Ma, X. Xu, Q. Li, Hierarchical $CoTiO_3$@NiO core–shell sub-microbelts as direct Z-scheme photocatalyst for efficient visible-light-driven tetracycline degradation, Appl. Surf. Sci. 546 (2021) 148892.

[45] P. Dhiman, A. Kumar, M. Shekh, G. Sharma, G. Rana, D.-V. N. Vo, N. AlMasoud, M. Naushad, Z. A. ALOthman, Robust magnetic ZnO-Fe_2O_3 Z-scheme hetereojunctions with

in-built metal-redox for high performance photo-degradation of sulfamethoxazole and electrochemical dopamine detection, Environ. Res. 197 (2021) 111074.

[46] M. E. Malefane, U. Feleni, P. J. Mafa, and A. T. Kuvarega, Fabrication of direct Z-scheme Co_3O_4/BiOI for ibuprofen and trimethoprim degradation under visible light irradiation, Appl. Surf. Sci. 514 (2020) 145940.

[47] H. Mohan, P. M. Sathya, S. Vadivel, G. Hyeon Ha, H. S. Oh, G. Kim, K.-K. Seralathan, T. Shin, Highly efficient visible light photocatalysis of $Ni_xZn_{1-x}Fe_2O_4$ (x = 0, 0.3, 0.7) nanoparticles: diclofenac degradation mechanism and eco-toxicity," *Chemosphere*, 301 (2022) 134699.

[48] Y. Nosaka, A. Y. Nosaka, Generation and detection of reactive oxygen species in photocatalysis, Chem. Rev. 117 (2017) 11302–11336.

[49] J. Madhavan, P. S. S. Kumar, S. Anandan, M. Zhou, F. Grieser, M. Ashokkumar, Ultrasound assisted photocatalytic degradation of diclofenac in an aqueous environment, Chemosphere 80 (2010) 747–752.

[50] C. Martínez, M. Canle L., M. I. Fernández, J. A. Santaballa, J. Faria, Aqueous degradation of diclofenac by heterogeneous photocatalysis using nanostructured materials, Appl. Catal. B. 107 (2011) 110–118.

[51] W. Li, R. Yu, M. Li, N. Guo, H. Yu, Y. Yu, Photocatalytical degradation of diclofenac by Ag-BiOI-rGO: kinetics, mechanisms and pathways, Chemosphere 218 (2019) 966–973.

[52] A. Ziylan, S. Dogan, S. Agopcan, R. Kidak, V. Aviyente, N. H. Ince, Sonochemical degradation of diclofenac: byproduct assessment, reaction mechanisms and environmental considerations, Environ. Sci. Pollut. Res. 21 (2014) 5929–5939.

[53] M. Elangovan, S. M. Bharathaiyengar, J. PonnanEttiyappan, Photocatalytic degradation of diclofenac using TiO_2-CdS heterojunction catalysts under visible light irradiation, Environ. Sci. Pollut. Res. 28 (2021) 18186–18200.

[54] J. Gou, Q. Ma, Y. Cui, X. Deng, H. Zhang, X. Cheng, X. Li, M. Xie, Q. Cheng, H. Liu, Visible light photocatalytic removal performance and mechanism of diclofenac degradation by Ag_3PO_4 sub-microcrystals through response surface methodology, J. Ind. Eng. Chem. 49 (2017) 112–121.

[55] Central Pollution Control Board (CPCB), General standards for discharge of environmental pollutants part-A: effluents, The Environment (Protection) Rules, India, 1986.

TABLE

Table 1 Leached metal ion concentration (in ppb) after photocatalytic degradation of PhACs onto FeCoNiCuZn under visible light irradiation.

	Fe^{2+}	Co^{2+}	Ni^{2+}	Cu^{2+}	Zn^{2+}
TC	229.62	73.05	228.56	1.12	61.91
SMX	175.74	80.58	189.52	5.12	65.37
IBP	123.48	121.68	125.46	21.78	72.86
DCF	129.45	102.36	132.3	5.54	67.23

FIGURES

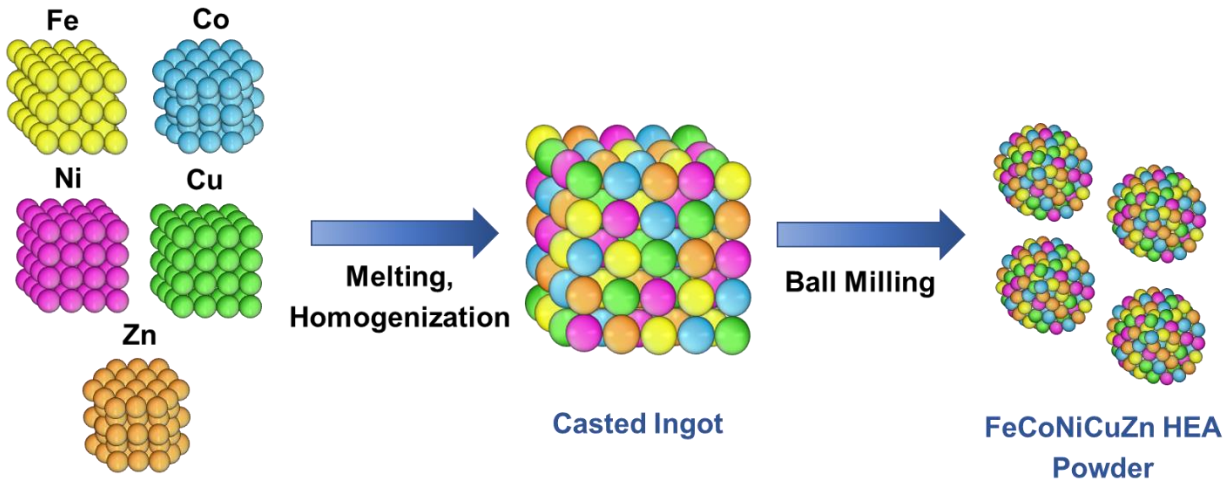

Figure 1 Schematic of the protocol for the synthesis of FeCoNiCuZn HEA powder.

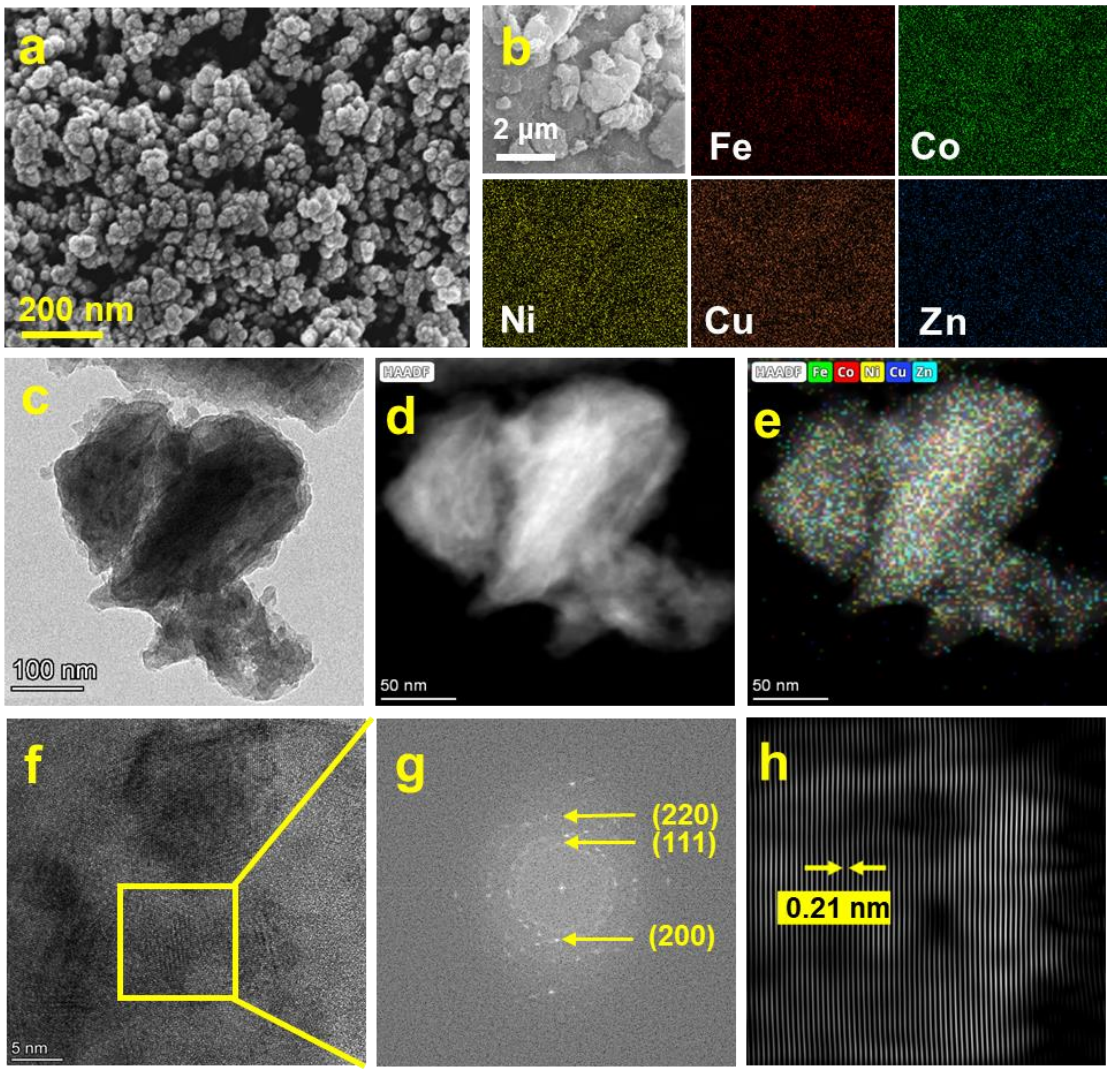

Figure 2 (a) FEG-SEM image of the synthesized FeCoNiCuZn HEA powder and (b) the corresponding EDS elemental mapping of the five individual elements present within the quinary HEA particle. (c) Bright-field TEM image of a FeCoNiCuZn HEA particle. (d) HAADF-STEM image and (e) the corresponding STEM-EDS mapping of FeCoNiCuZn HEA particle. (e) HRTEM image and (f) the corresponding FFT pattern of FeCoNiCuZn HEA particle. (g) HRTEM of FeCoNiCuZn HEA particle illustrating the measured lattice fringe spacing.

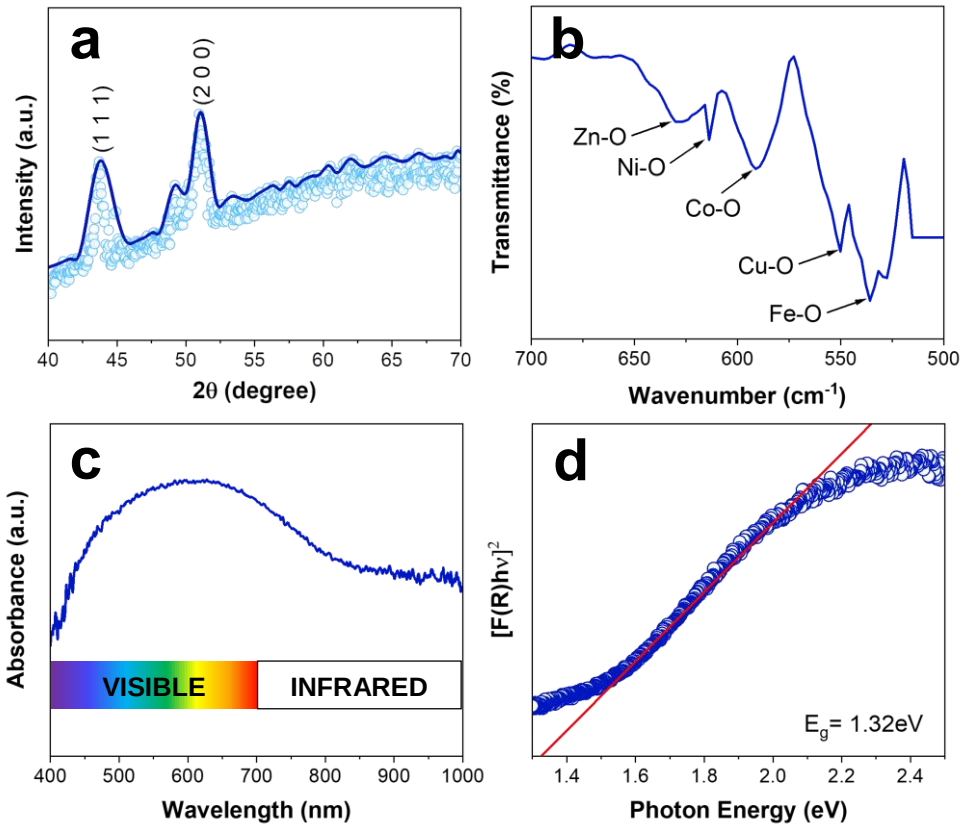

Figure 3 (a) XRD pattern clarifying the crystal structure of the FeCoNiCuZn HEA. (b) FTIR fingerprint depicting the surface chemistry of FeCoNiCuZn HEA particle. (c) UV/Visible absorbance spectrum of the synthesized FeCoNiCuZn HEA powder in diffuse reflectance mode and (d) the Kubelka–Munk plot for the estimation of the bandgap energy.

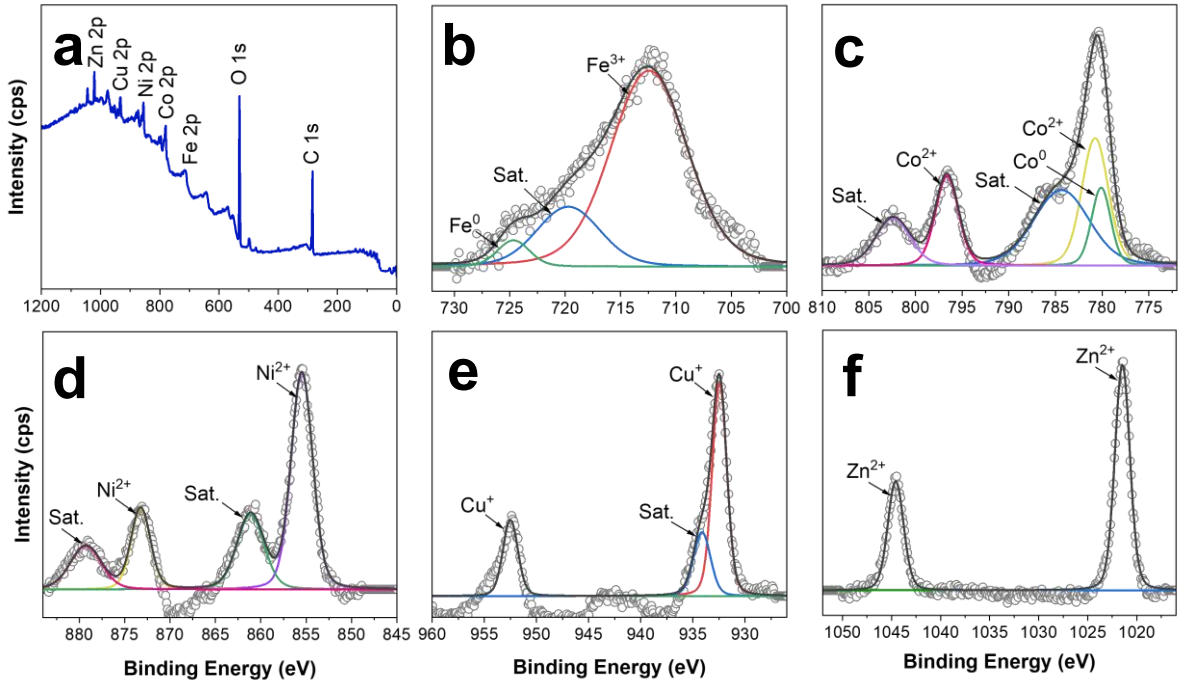

Figure 4 (a) XPS survey scan and deconvoluted high-resolution (b) Fe 2p, (c) Co 2p, (d) Ni 2p, (e) Cu 2p, and (f) Zn 2p spectra of the as-synthesized FeCoNiCuZn HEA, showing the oxidation state of the constituent elements.

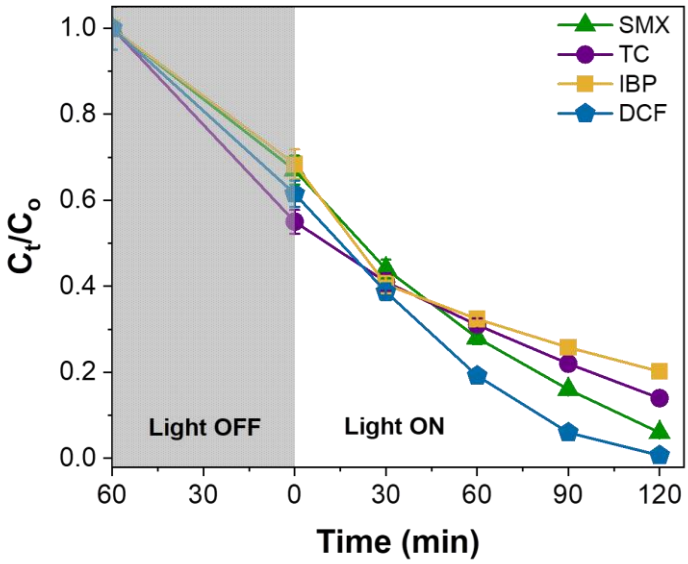

Figure 5 Visible light-induced photocatalytic degradation of TC, SMX, IBP, and DCF onto the FeCoNiCuZn HEA (experimental conditions: C_0 = 5 mg L^{-1}; photocatalyst dose = 0.5 g L^{-1}; temperature = 25 ^{o}C).

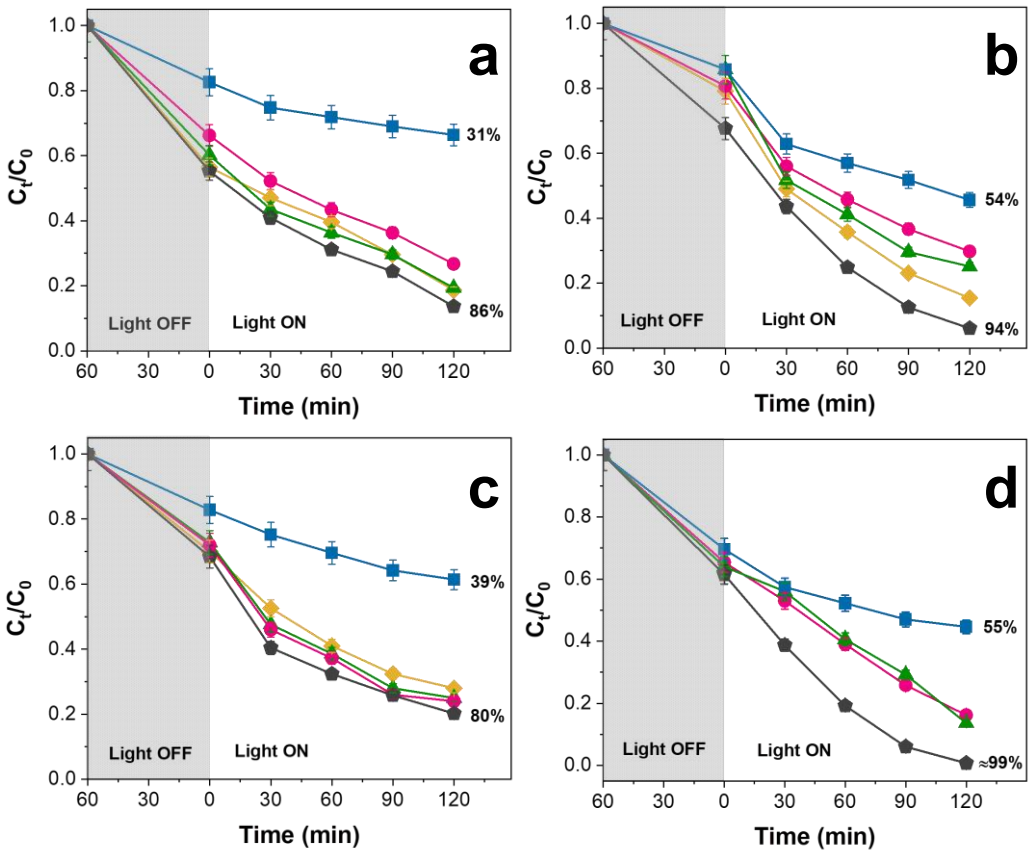

Figure 6 Photocatalytic degradation of (a) TC, (b) SMX, (c) IBP, and (d) DCF over FeCoNiCuZn HEA under visible light irradiation with and without different ROS scavengers and hole quencher (◆ NaN_3, ● IPA, ▲ KI, ■ AA, ⬟ No Scavenger)

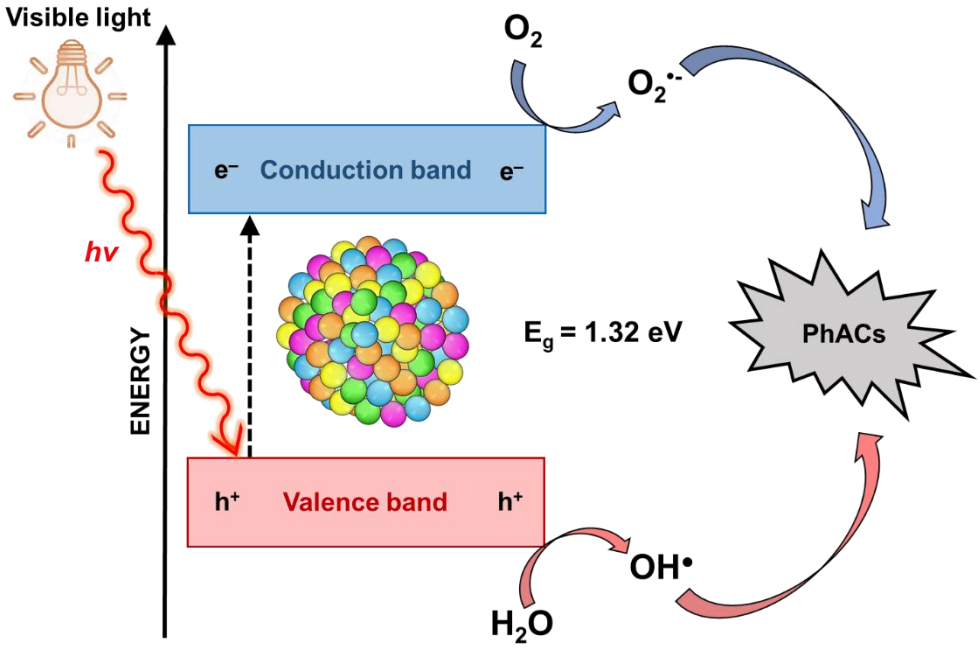

Figure 7 Schematic of the plausible photocatalytic degradation mechanism of FeCoNiCuZn HEA under visible light irradiation.

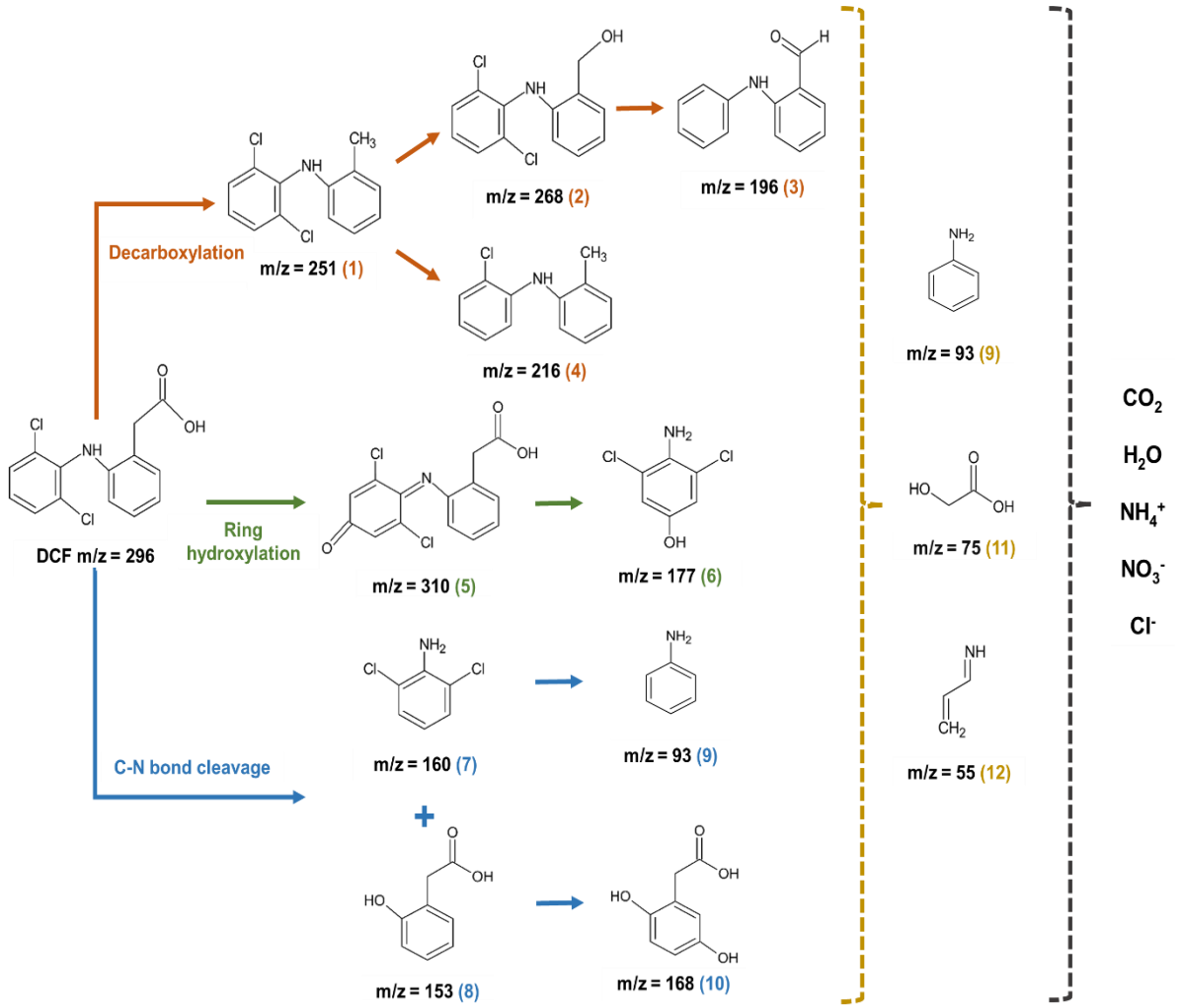

Figure 8 Proposed pathway for degradation of DCF over the synthesized FeCoNiCuZn HEA under visible light irradiation.

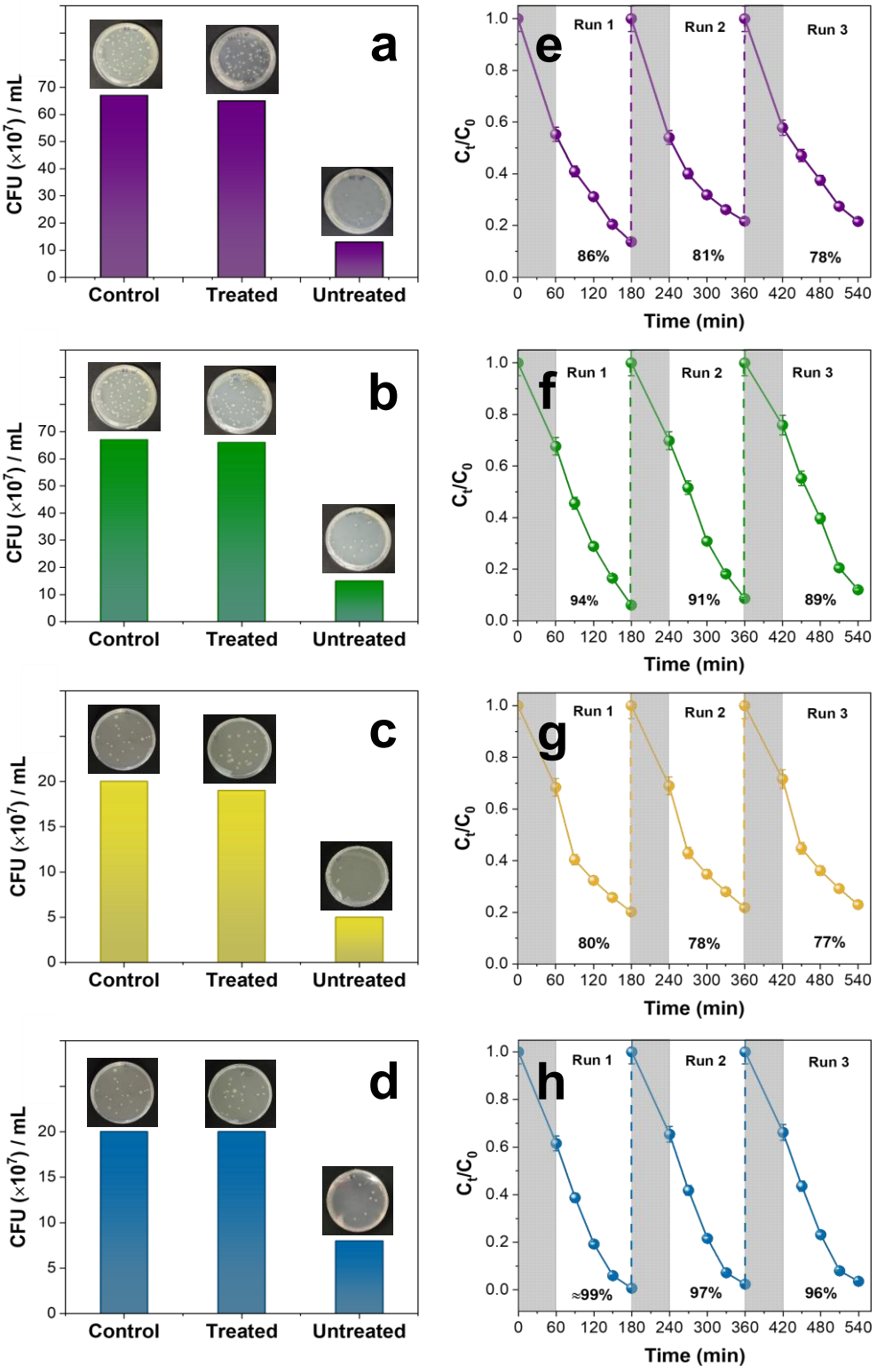

Figure 9 Toxicity evaluation of treated and untreated (a) TC, (b) SMX, (c) IBP, and (d) DCF solution toward *E. coli* with respect to deionized water. Reusability of FeCoNiCuZn HEA for photocatalytic degradation of (e) TC, (f) SMX, (g) IBP, and (h) DCF.

GRAPHICAL ABSTRACT

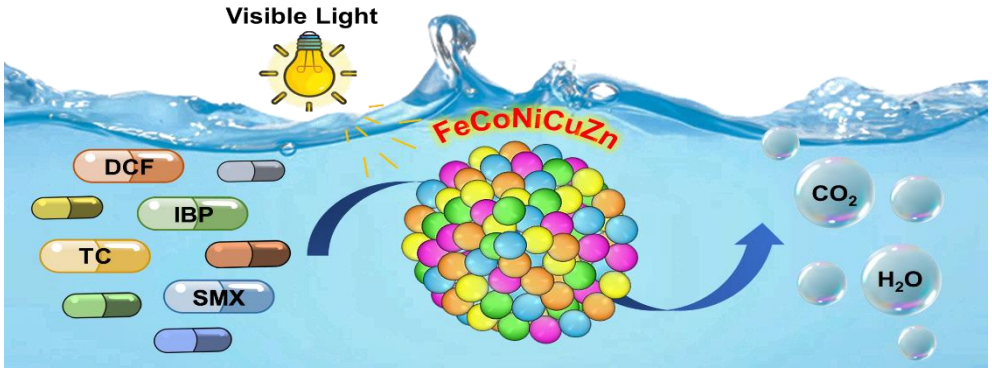

HIGHLIGHTS

- An equimolar FeCoNiCuZn high entropy alloy (HEA) is synthesized by induction melting
- The quinary HEA can effectively degrade pharmaceutical residues under visible light
- The plausible photocatalytic degradation mechanism is investigated and proposed
- The photocatalysis end-products do not present any imminent threat to human health
- The HEA exhibits extraordinary stability for repeated usage